Fire Safety Journal 141 (2023) 103907

Contents lists available at ScienceDirect

Fire Safety Journal

journal homepage: www.elsevier.com/locate/firesaf

CFD informed design of bench-scale experiments to characterize air entrainment into fuel beds induced by columnar vortices

Giovanni Di Cristina *, Rodney A. Bryant

National Institute of Standards and Technology, Fire Research Division, Engineering Laboratory, Gaithersburg, MD, USA

A R T I C L E   I N F O

Keywords:
Buoyancy-induced flow
Computational fluid dynamics
Air entrainment
Fire-induced flow
Spot ignitions

A B S T R A C T

Recent experiments show that strong vortices, similar to fire whirls, can form far from a fire front in the region of smoldering fuel. These buoyancy-induced columnar vortices, visualized by entrained smolder smoke, were observed lofting hot embers into the air and in some cases lead to spot ignitions at the base of the vortex. Gaining insight on how the flow field of a buoyancy-induced columnar vortex could impact surrounding smoldering fuel is the focus of this study. Specifically, the potential air entrainment into a fuel substrate beneath the vortex. The flow field of such columnar vortices has been shown to drive air flow downward under certain conditions and, in the context of combustion, drive air deeper than typical entrainment, inducing spot ignitions and increasing burning and smolder rates. NIST's Fire Dynamics Simulator is utilized to successfully model buoyancy-induced columnar vortices. Then it is utilized to study the behavior of vortices as temperature and vorticity boundary conditions are changed. The flow field and fresh air entrainment potential are analyzed. The simulation results inform the experiment design and preliminary experimental results are presented. Understanding these high-risk phenomena will lead to better risk mitigation and more resilient Wildland-Urban interface communities.

1. Introduction

The severity of wildland fires has been increasing since 2011 [1]. In 2021, some of the longest active wildland fires on record occurred [1]. Although nationally the number of fires and acres burned were on par with the 10-year average, fire prone areas such as California saw the number of acres burned exceed the 10-year average by 160%. Furthermore, an increase in acres consumed while the number of fires remained on average is indicative of increasing fire severity and risk. As fire severity grows, the interactions and coupling between the fire-induced flow and the atmospheric wind produce increased turbulence and can lead to the formation of dangerous phenomena. Examples of such phenomena can be seen in fire whirls [2] and fire storms [3,4]. The increase in fire severity and higher probability for dangerous vortices to form poses an increasing risk for communities at the wildland-urban interface (WUI), as evidenced by the Marshal Fire in Colorado in 2021. The fire burned over 1000 residences in a few hours due to an extreme wind event and was ultimately deemed the year's most destructive wildland fire [1]. The need to better understand and model these phenomena will lead to more fire resilient communities and better risk mitigation [5].

A fire whirl is a type of extreme fire phenomenon formed through the coupling of wind and flames. It is a buoyancy-induced columnar vortex (BICV) formed through the hot gasses rising from the flame and interactions with vorticity from the surroundings, either from terrain or obstacles such as structures or vegetation [2]. Recent experiments showed that vortices, similar to fire whirls, can form far from the fire front in the region of smoldering fuel. The columnar vortices occurred during tests under no wind conditions in the test section of a large-scale wind tunnel [6]. The overall fuel bed dimensions were 5 m × 1 m and smoke whirls were observed at fuel loadings ranging from 0.5 to 1.5 kg/m^2. These buoyancy-induced columnar vortices were visualized by the smoke from the smoldering pine needle fuel bed. Accompanying the formation of the BICV above the smoldering fuel were spot ignitions at the base of the vortex. Fig. 1 provides a schematic (Fig. 1c) of the BICV formation behind a fire front along with images showing a BICV behind a fire. Fig. 1a is reproduced from literature [2] and shows the BICV formation behind a burning structure. Fig. 1b shows the BICV above a smoldering fuel bed observed in recent experiments. Similar to Fig. 1a, the BICV is in the wake of a flame front. These observations over a wide range of size scales provides motivation for this study.

However, BICVs are not unique to wildland fires. Such interactions between rising warm currents of air and the atmosphere include dust-

* Corresponding author.
E-mail address: giovanni.dicristinatorres@nist.gov (G. Di Cristina).

https://doi.org/10.1016/j.firesaf.2023.103907
Received 23 May 2023; Received in revised form 23 July 2023; Accepted 14 August 2023
Available online 17 August 2023
0379-7112/Published by Elsevier Ltd.

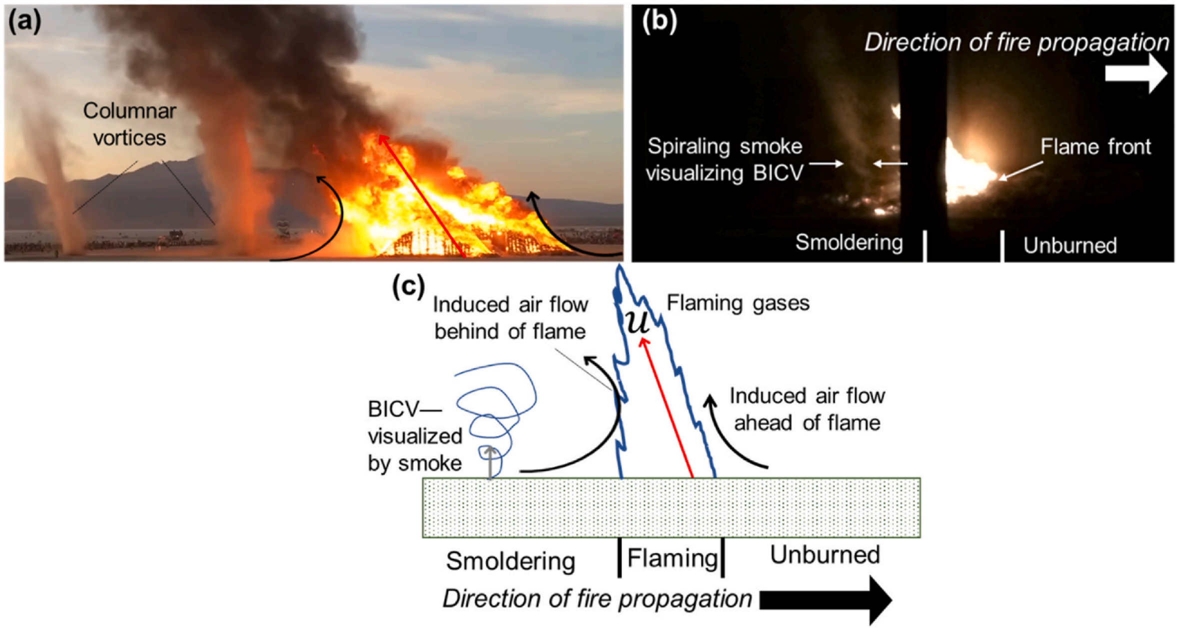

Fig. 1. Sketch of the columnar vortices observed in previous experimentsof fire spread along pine needle fuel beds. The interaction between the upward buoyant air from the flame and the induced lateral entrainment generated the whirling motion. On the left (a), an image adapted from Ref. [2] showing columnar vortices in the wake for a building fire.

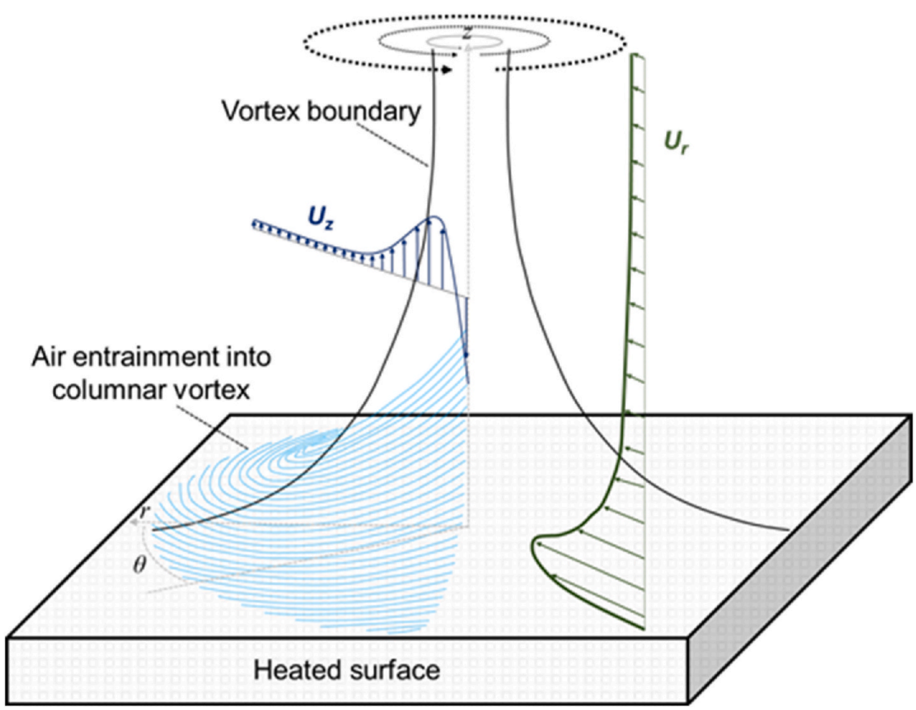

Fig. 2. Flow field of columnar vortex adapted from Tohidi et al. [2]. U_z is the vertical velocity and U_r is the radial entrainment velocity. The heated surface can be provided through radiation (dust devils) or smoldering (wildland fire) which provide the buoyant updraft needed to induce the vortex formation.

Table 1
FDS setup parameters for the simulations of the large (1 m) and small (0.3 m) heaters.

	Large Heater	Small Heater
Heater length	$L_h = 1$ m	$L_h = 0.3$ m
Vane length (l)	35 cm	11.67 cm
Vane Angle (θ)	30°, 50°	30°, 50°
Computational Domain (S x S x S)	1 m × 1 m x 1 m	0.5 m × 0.5 m x 0.5 m
Grid resolution	1 cm	0.2 cm
Heater Area	1 m^2	0.09 m^2

devils, waterspouts, and on a mesoscale - hurricanes and tornadoes. When upward moving buoyant air and lateral air entrainment interact, rotating columnar vortices form. Dust-devils, in particular, have been utilized as a way to inform the prediction and modelling of hurricanes and tornadoes [7–17]. Laboratory experiments have examined the formation [9,15] and sought to characterize the flow-field of BICV [8]. It was found that in order for a BICV to form, a source of buoyancy and a source of vorticity are needed. In the case of a dust-devil, the buoyancy is provided by the hot surface found in dessert environments [15]. The vorticity is generally formed in the interactions between the terrain and the atmospheric boundary layer [7]. In laboratory experiments, free-standing vortices, or vortices formed on open surfaces without vanes, are difficult to generate reliably and consistently. Researchers generally use different mechanical means of introducing vorticity such as radially distributed vanes [8,9], rotating screens [18,19], or offset cylindrical air intakes [20].

Mullen and Maxworthy [9] documented the different BICV core structures by utilizing a heated plate and radially distributed vanes to artificially induce the vortex. Their research showed the interaction of the heat source and vane generated vorticity formed either a single cell (1-cell) or double cell (2-cell) vortices, as determined by the flow in the core region. The single-celled vortices feature strong upward flows in the core region, while two-celled vortices have a downdraft in the core region. Depending on the conditions, a single-celled vortex may break down into a two-celled structure [7,9,21]. More recent experiments by Simpson [8,21] expanded on the setup utilized by Mullen and Maxworthy with particle image velocimetry to measure the entire flow field. A connection between the Grashof number and the angle of the vanes was identified which determined if the vortex that formed would be a single or double celled structure. Varaskin [11–13] has been able to reliably generate BICVs without mechanical sources of vorticity. Although Varaskin did not characterize the core structure of the vortices explicitly, temperature and velocity measurements show lower values in the core region under different heating modes. Fig. 2 shows a qualitative flow field of a buoyant columnar vortex adapted from the literature [2, 8–10,14,22].

The vortices previously observed above smoldering pine needles were too small to identify the core structure, however, the spot ignitions are hypothesized to be caused by downward air currents resulting from BICV formation. The cooler air brought downward either in the core region resulting from a two-celled vortex or in the entrained air near the

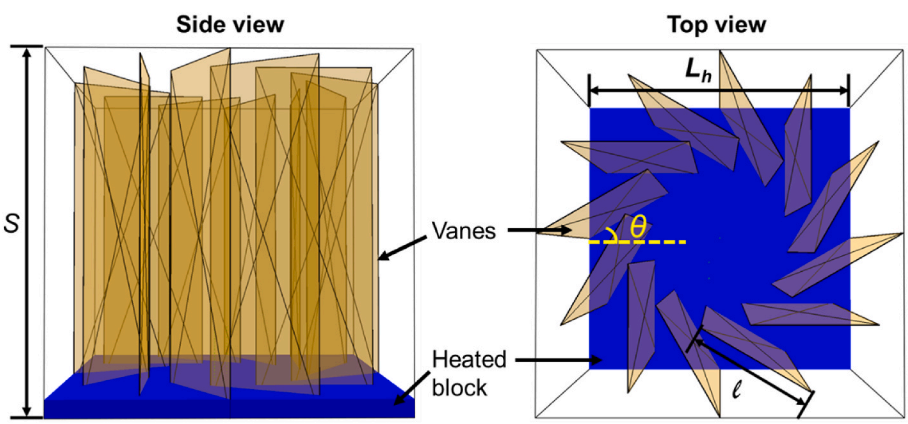

Fig. 3. FDS domain and setup. The various simulations featured a heater at the base of the domain and radially distributed vanes.

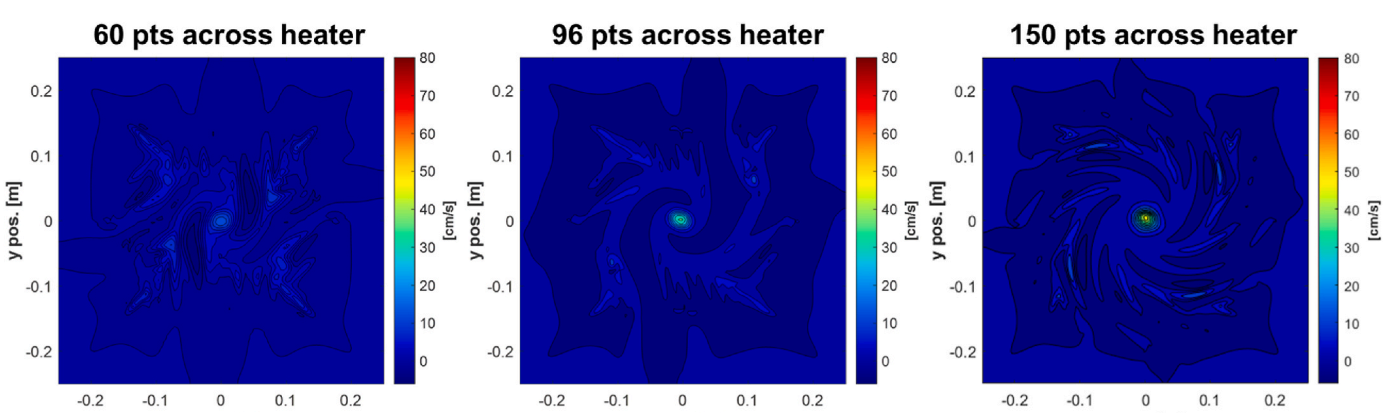

Fig. 4. Total velocity contours of the mesh study results for the $L_h = 0.3$ m heater. Adequate modelling of the vortex was achieved at 96 cells across the heater, but 150 cells provided better resolution.

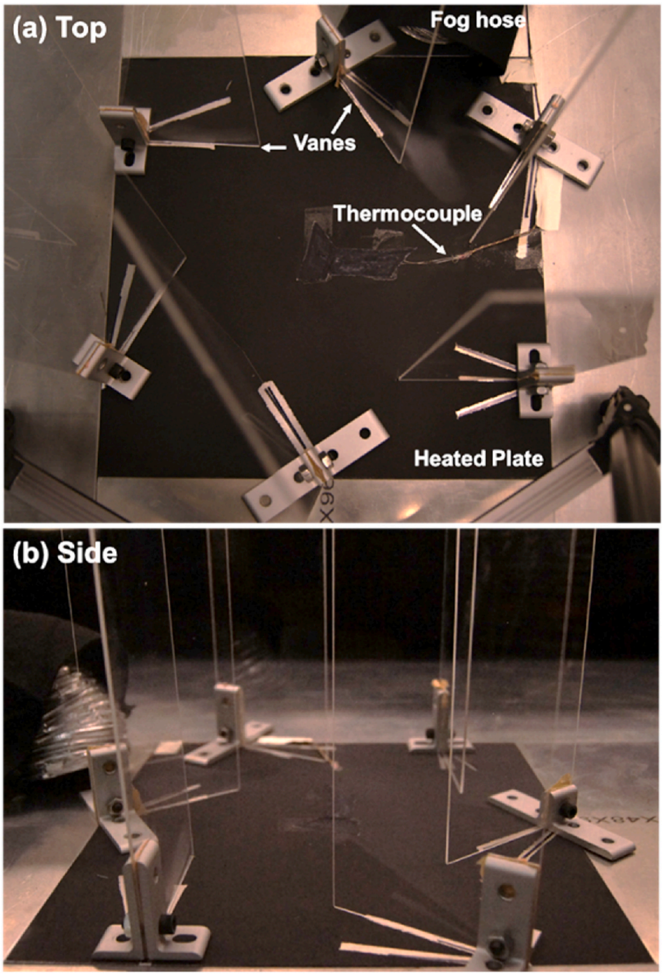

Fig. 5. Images of the experimental setup (a) top and (b) side views. Shown is the 6-vane configuration at 30° radially distributed on the heated plate and the thermocouple for heater control.

fuel surface then penetrates the smoldering fuel providing oxygen to a fuel rich regions and transitioning from smoldering to flaming [23]. Canonical fire whirls have been shown to increase the combustion efficiency measured through the mass consumption of fuel [24]. Although in the context of wildland fire, BICVs have largely been studied through fire whirls, recent studies have shown that flameless 'whirls' are formed in the wake of fires as a result of coupling between the ambient cross-wind and the flame induced currents [25].

Gaining insight on how the flow field of a BICV impacts surrounding smoldering fuel is the focus of this study. Specifically, the air entrainment into a fuel substrate caused by BICVs. However, this investigation does not feature a combustion reaction. Instead, previously published dust devil experiments [8,9,21] were simulated using NIST's Fire Dynamics Simulator (FDS) [26]. FDS provides insight to the flow physics necessary to establish stable, single cell (1-cell) or double cell BICV core structures. The FDS results were validated using previously published results and flow visualization methods presented herein. FDS was subsequently used to assess the impact of experimental control parameters (*e.g.*, heat input, induced vorticity) on the structure of the BICV including its core structure and the downward flow outside the vortex core. The results of the assessment guided the use of FDS to simulate a smaller whirl generator. Successful simulation of BICVs at the smaller scale then guided the design of a bench-top whirl generator. Preliminary results from the bench-top experiment are presented. These results demonstrate the successful use of FDS to guide experimental design.

2. Methods and materials

2.1. FDS simulations

Laboratory studies of dust devils have been described by Mullen and Simpson [8,9]. In their experimental work a heated plate was set to a constant heat flow [9] or temperature [8]. Radially distributed vanes, 0.5 m from the center (1 m radius), gave the induced flow a swirl and vorticity which resulted in the formation of a columnar vortex in the center. Smoke visualization along with a range of measurements were taken in each study. The experiments are of appropriate physical scale to model with computational fluid dynamics (CFD) at the desired grid resolution and with reasonable computing resources. Because the BICV are flameless (reactionless), the dust devil is an apt comparison, as the fluid mechanics are similar. FDS, which utilizes a 3-dimensional Large Eddy Simulation (LES) [26,27] scheme to solve the Navier-Stokes equations, was applied to model the dust devil experiments. FDS was designed for fire modelling, as such, numerical models are incorporated for gas-phase combustion, thermal radiation, and solid fuel burning behavior; however, this study does not incorporate any combustion reaction or fuel. The near wall flows are resolved through a log-law model with an immersed boundary for flow obstacles. The model determines the tangential velocity component in the first off-wall cell based on if the location is in the viscous sublayer (linear) or not (logarithmic profile). The sub-grid turbulence is resolved through an eddy viscosity (Deardoff's eddy viscosity model) model. Further details on FDS, including model validation, can be found in the technical documentation [26,27].

The literature experiments utilized a heated plate, 1 m × 1 m, with vanes distributed radially about the plate to generate vorticity. The results of these experiments are used to validate the FDS simulation and confirm it as a suitable scheme to model BICV. Two heater sizes (L_h) are simulated, 1 m and 0.3 m. The small scale heater, $L_h = 0.3$ m, was chosen as the target size for further laboratory experiments. The FDS simulations are utilized as a tool to study the scaling of BICVs with respect to parameters controlling heating and vorticity and inform the design of successful experiments. Table 1 shows the dimensions of the domain setup for each scale tested. The vane lengths were scaled down linearly from a Grashof number (*Gr)* similarity based on the heater size, and the vane locations were kept at the edge of the heater perimeter.

Fig. 3 shows side and top views of renderings from the simulation domains, as well as a diagram indicating domain length (S), heater length (L_h), and vane angle (θ), and vane length (l).

At each heater scale, simulations were conducted for 120s at multiple vane configurations – no vanes, with vanes at angles (θ) of 30°, and 50°, and multiple heater temperatures - 50 °C, 100 °C, and 150 °C. The heater temperatures chosen reflect those that were utilized in the literature [8, 9]. Simulations for the large and small heaters feature a uniform grid with 1 cm and 0.2 cm mesh grid cell resolution, respectively.

Based on a mesh study, each domain needs at least 100 grid points across the heater to adequately simulate the vortex rotation. For the $L_h = 1$ m case, 100 cells gave a good vortex resolution, however, for the $L_h = 0.3$ m simulations, increasing to 150 grid cells across the heater gave improved vortex results (Fig. 4) with marginal computational cost. For all simulations the boundary conditions for the sides and top were set as open boundaries, enabling the flow of gasses in and out of the domain. The $L_h = 1$ m simulations employed 12 vanes; however, the $L_h = 0.3$ m simulations were conducted for 6 and 12 vanes since the laboratory experiments employ 6 vanes to facilitate optical access into the center.

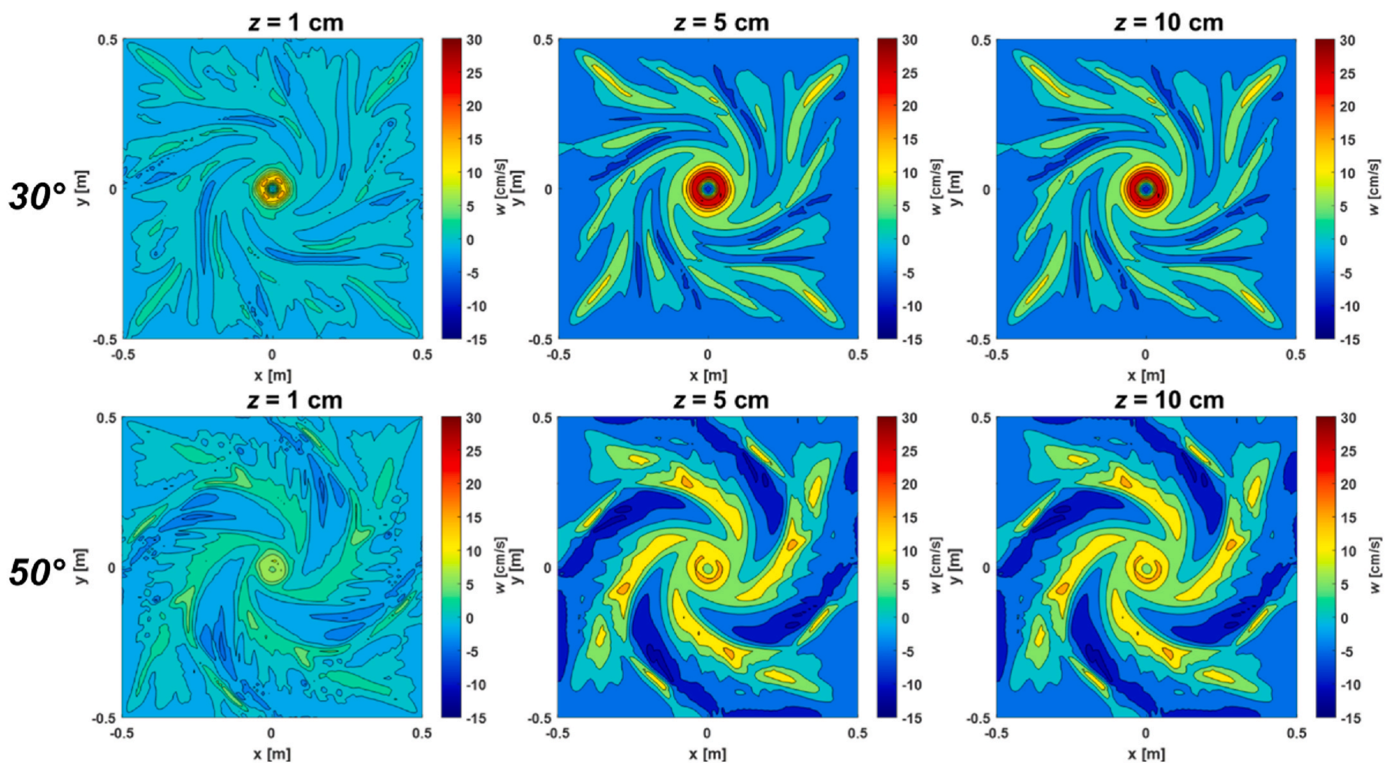

Fig. 6. Vertical velocity component (w) contours for the horizontal plane (xy) at various heights above the heater ($z = 1$, 5, 10 cm) and vane angles. Contours are for the $L_h = 1$ m case at a heater temperature of 100 °C. Contours show the 90s time average.

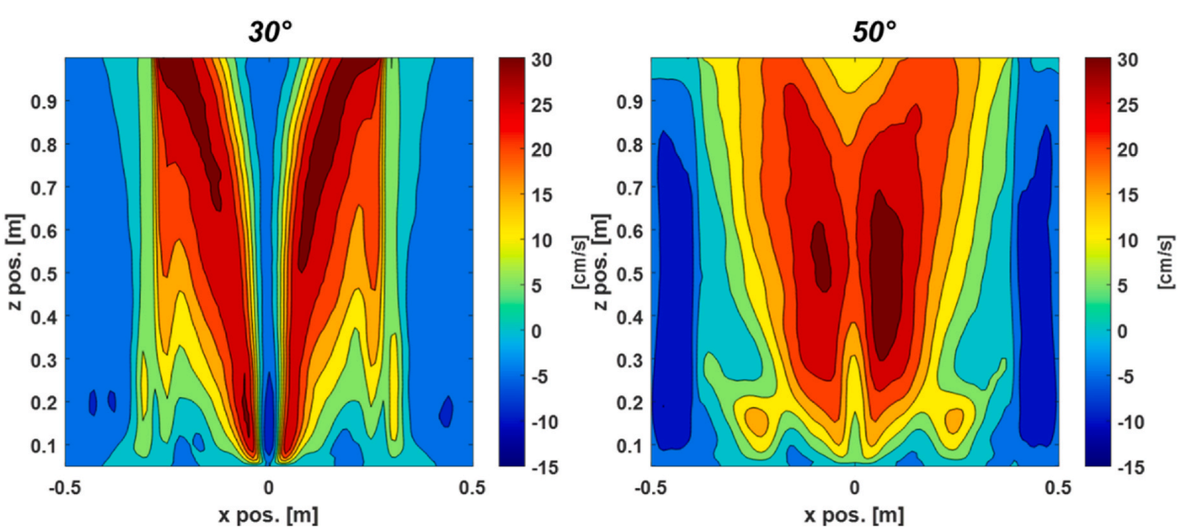

Fig. 7. Vertical velocity component (w) contours of the vertical plane (xz) along the centerline ($y = 0$ cm) of the $L_h = 1$ m domain for 30° (left) and 50° (right) vane angle cases.

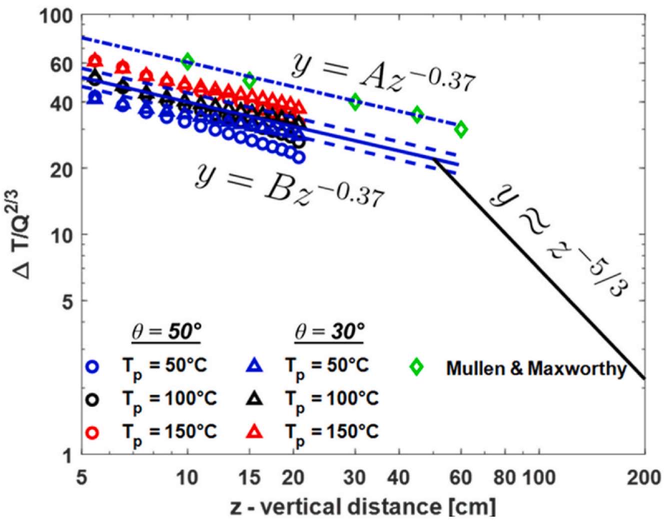

Fig. 8. Height evolution of the centerline temperature scaled by the heat input. FDS results for the $L_h = 1$ m cases are compared to literature results and a canonical buoyant plume. Blue dashed lines represent 10% error bands of the power-law relationship for visualization. (For interpretation of the references to color in this figure legend, the reader is referred to the Web version of this article.)

2.2. Bench-top experiment

The FDS results supported the design of benchtop experiments, as the setup is based on the small-scale simulation (Table 1). The overall design is a 1 m × 1 m table comprised of aluminum sheets. A 30 cm × 30 cm aluminum plate sits in the center of the table and is heated using strip heaters (Omega, Model SRFGA-218/5).[1] The heaters are 10 cm × 38 cm and are arranged side by side with a spacing of 5 cm from the edges of the heater and each other. A PID controller (Omega, Model CNi16D33) drives the heaters simultaneously. A thermocouple (Type K), mounted on top of the aluminum plate and at the center of the heated region, provided feedback to the PID controller. Fig. 5 shows images of the experimental setup from the top and side views.

To facilitate camera access, only six vanes were used to generate vorticity. They were placed around the perimeter of the heated plate at the same radial distance as defined in the simulations. Preliminary experiments consist of visualizing the BICVs by seeding surrounding air with fog particles. The fog (water-ethylene glycol) was generated using a fog generator (Rosco 1700). Video imaging of the seeded flow was acquired at 30 Hz using a digital camera (Sony A55).

3. Results and discussion

Qualitative features of the flow field were consistent across heater temperatures. Therefore, the results of the 100 °C heater temperature were chosen as the representative case for discussion. However, in instances of discussing overall trends, the results from the other heater temperatures are referenced.

[1] Certain commercial entities, equipment, or materials may be identified in this document in order to describe an experimental procedure or concept adequately. Such identification is not intended to imply recommendation or endorsement by the National Institute of Standards and Technology, nor is it intended to imply that the entities, materials, or equipment are necessarily the best available for the purpose.

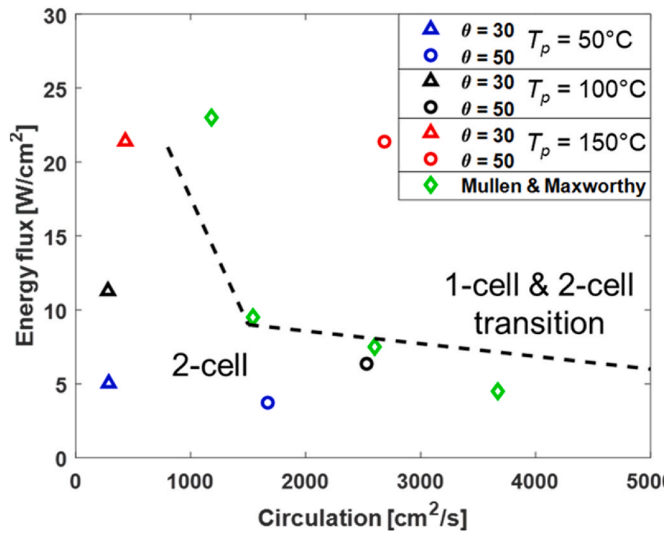

Fig. 9. Regime map developed by Mullen [9] plotted alongside the $L_h = 1$ m FDS results for various vane angles.

3.1. $L_h = 1$ m

Fig. 6 shows the time-averaged vertical velocity (w) contours for the horizontal (xy-plane) at two vane angle conditions (30° and 50°). The simulations reach a quasi-steady state at approximately 15s. To remove startup effects the contours are the average of the last 90s of simulation. The contours correspond to 1 cm, 5 cm, and 10 cm above the heater surface.

The contours show strong swirling motion across all cases with vanes. As air is heated at the surface, it rises and entrains fresh air through the vanes. The vanes then impose a swirl angle and introduce vorticity. Entrained air at the surface of the heater and at the base of the BICV has a strong downward motion. At 1 cm above the heated plate, downward entrainment regions (blue), radially distributed from the center, can be observed in Fig. 6. In the 30° case there are approximately 8 regions defined by the blue streaks of negative vertical velocity, while the 50° case features 4 larger regions. As the height increases, the streaks in the 30° case begin to resemble the 50° case. For the 30° case, downward velocities are prominent in the core region of the vortex. This is indicative of the formation of a 2-cell vortex structure as defined by Mullen and Maxworthy [9].

The 2-cell vortex structure is easily visualized from the vertical velocity contours taken from the vertical (xz plane) at centerline ($y = 0$ cm), Fig. 7. The 50° case does not feature a downward flowing column in the vortex core as prominent as the 30° case. However, the time resolved results show that the center fluctuates between downward and upward modes, indicative of a transitional condition between the 1-cell and 2-cell regimes at the 50° case.

3.2. Literature comparison

The temperature decrease for a buoyant plume can be characterized by the following power-law relationship [9]:

$$\frac{\Delta T}{Q^{2/3}} \propto z^{a} \tag{1}$$

where Q is the heat input [kW] into the system, ΔT is the difference between the centerline temperature and ambient, z is the vertical height [m] and a is the empirical constant describing the system. The scaled temperature results from the literature and FDS are plotted in Fig. 8.

A purely buoyant plume is characterized by a = -5/3, plotted for

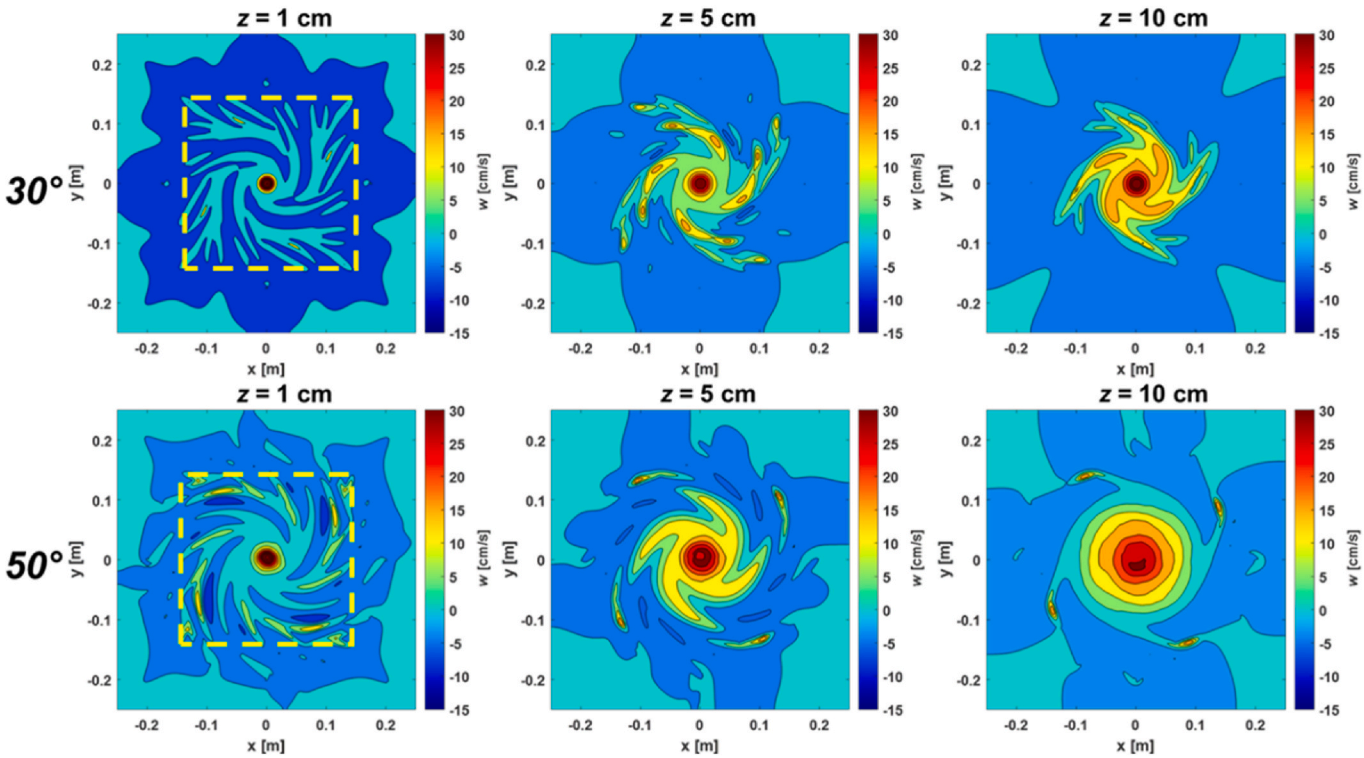

Fig. 10. Vertical velocity (w) contours for the horizontal plane (xy) at various heights (z) above the heater and vane angles. Contours are for the $L_h = 0.3$ m at 100 °C case; show the 90s time average; and the heater is indicated by the dashed outline.

reference in Fig. 8. The results from Mullen and Maxworthy [9] showed that when a BICV forms, the temperature evolution follows an exponent of $a = -0.37$. In contrast to a purely buoyant plume that expands as it flows upwards, a vortex constrains the higher temperature gases in the center, thus limiting the diffusion and expansion into the surroundings. The FDS results, plotted in Fig. 8, align the power-law relationship described in Eq. (1). This is indicative of vortex formation and accurate representation of the vortex dynamics. As the results from different temperature cases show, the proportionality coefficient of Eq. (1) scales with the temperature difference induced by the heat source.

Further validation of FDS can be obtained by examining the vortex behavior regimes. It was reported by Mullen [9] that the vortex behavior regimes can be mapped in terms of the circulation and energy flux. It is critical to note here that the energy flux defined by Mullen was a function of the heat input divided by the square of the vortex radius, Q/r^2. The results from the $L_h = 1$ m simulations are plotted in Fig. 9 in terms of the Mullen defined energy flux and the calculated circulation. The 30° vane case lies staunchly in the mapped 2-cell vortex regime, as confirmed by the velocity contours. The 50° vane case lies on the transition between a 1-cell and 2-cell vortex condition. This is consistent with the averaged velocity contours and the time resolved results fluctuating between a 1-cell and 2-cell vortex structure.

3.3. $L_h = 0.3$ m

The small-scale heater was chosen to fit within a benchtop experimental setup and therefore was the driving dimension to scale down the simulation. Vertical velocity (w) contours for the small-scale heater are shown in Fig. 10. The contours are for the same conditions as the ones shown for the $L_h = 1$ m case (Fig. 2). The dashed outline indicates the heated plate.

A columnar vortex was successfully simulated at the smaller scale, with rotating structures observed similar to the literature scale simulations. Moreover, the downward entrainment streaks observed radially surrounding the vortex core are also present. The streaks gradually diminish with height above the surface. Unlike the $L_h = 1$ m cases, there are no signs of a 2-cell vortex. However, significant downward entrainment still occurs outside of the vortex core region.

Fig. 11 shows a comparison of the contours between the two scales at a height of 1 cm above the surface. The vortex core region velocities for the $L_h = 0.3$ m case are much higher, reaching around 30 cm/s while the $L_h = 1$ m case are shown to be around 10–15 cm/s. The vortex core radius shrank from approximately 5 cm ($L_h = 1$ m) to 2.4 cm ($L_h = 0.3$ m).

3.4. Downward entrainment

As a BICV forms over the smoldering fuel, downward mass flow injects fresh air into a substrate, such as smoldering pine needles. The added oxygen from the entrained air leads to an increase in spot ignitions as smoldering regions transition to flaming. Entrainment into a smoldering substrate was characterized by computing downward mass flow at 1 cm above the heater surface. The results for the downward mass flow measurements are shown in Table 2. These results include additional cases that use 6 vanes as well as a baseline case of no vanes for comparison.

In general, the formation of a BICV increased the downward entrainment as compared to the no vane case. This can be attributed to

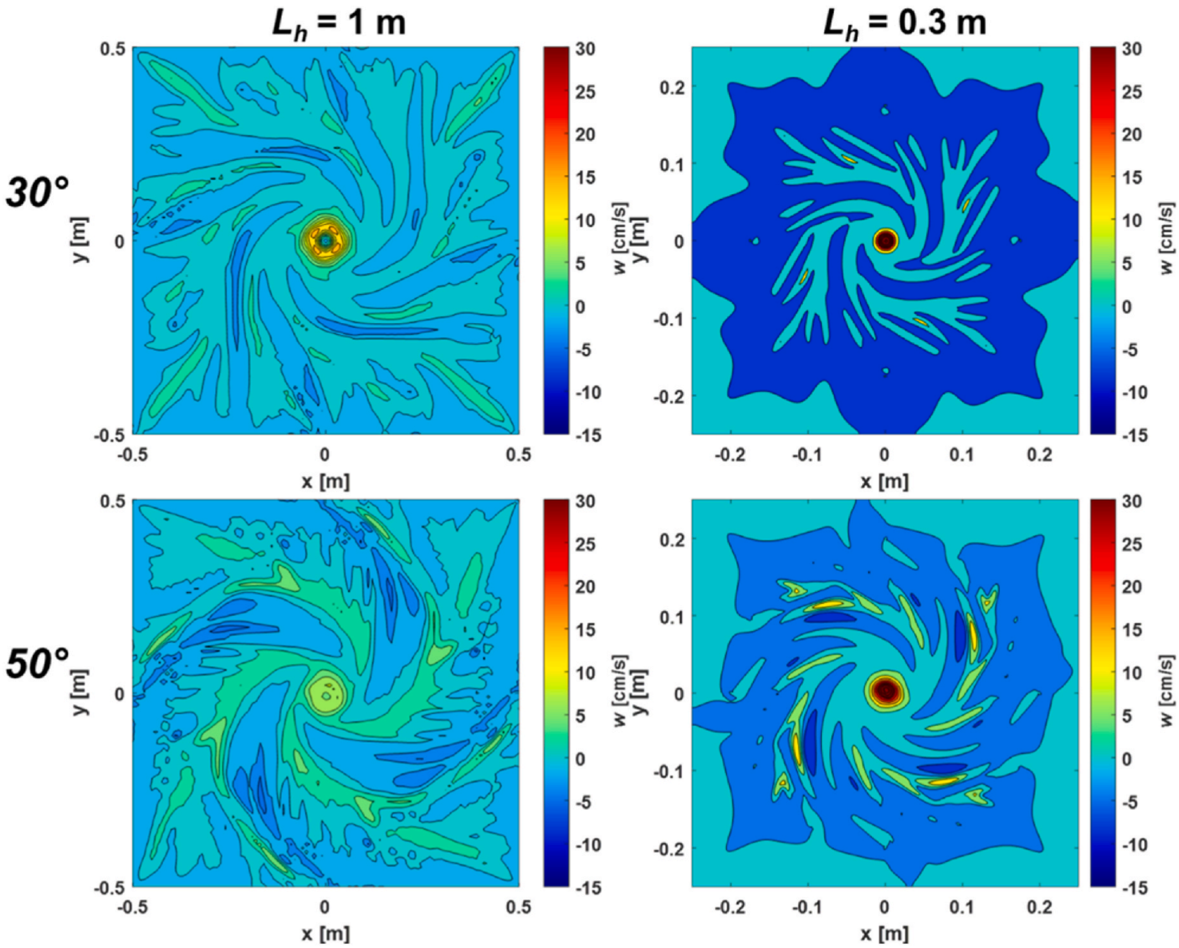

Fig. 11. Comparison of FDS results of average vertical velocity (w) at $z = 1$ cm and 100 °C heater temperature.

Table 2
Downward mass flow results for 100 °C heater temperature.

L_h [m]	Vanes	θ	Total downward mass flow [g/s]	Mass Flux [g/m^{2}s]	Δ [%]
1	No Vanes		2.66	2.66	
	12	30°	4.94	4.94	86
		50°	6.21	6.21	133
	6	30°	3.88	3.88	46
		50°	4.25	4.25	60
0.3	No Vanes		0.75	3.01	
	12	30°	1.34	5.36	78
		50°	1.57	6.29	109
	6	30°	1.16	4.64	54
		50°	1.21	4.82	60

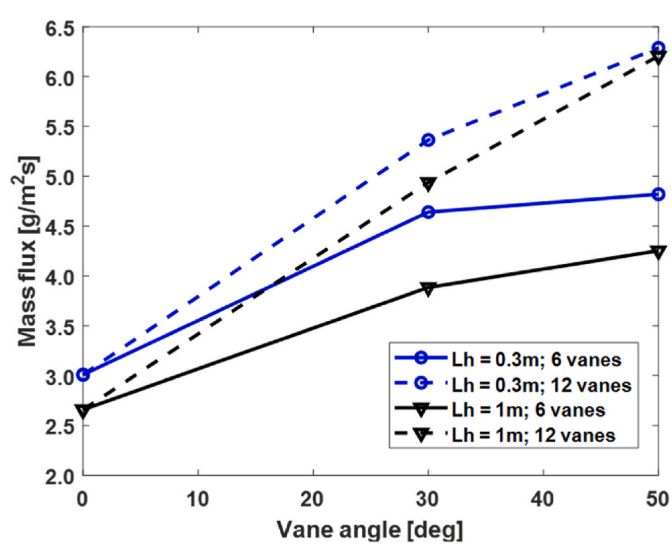

Fig. 12. Mass flux results plotted against vane angle. Additional parameters are heater size and number of vanes.

the entrainment streaks that form radially in the presence of a vortex, as shown in the vertical velocity contours, as well as the 2-cell structure that formed under certain conditions. Increasing the vane angle leads to greater downward entrainment, while fewer vanes lead to lower downward entrainment due to reduced vortex intensity. In order to account for the difference in domain areas, the mass flux was calculated. In this way, it is seen that the downward mass flow follows a similar trend. Fig. 12 plots the mass flux for the different vane angle conditions, with the 0° vane angle point representing the no vane conditions.

As vane angle increases, the downward mass flux tends to increase. Likewise, the number of vanes also contributes to an increase in downward mass flux. As the number of vanes is reduced to 6, the increase in vane angle from 30 to 50° results in only a slight increase in the mass flux of 6% and 14% for the small and large heaters, respectively, while the 12 vane cases result 31% and 47% increases. As more vanes are added, more of the air that is entrained through the vanes is turned since the gap between vanes is smaller. With fewer vanes, the impact of the vane angle is minimized.

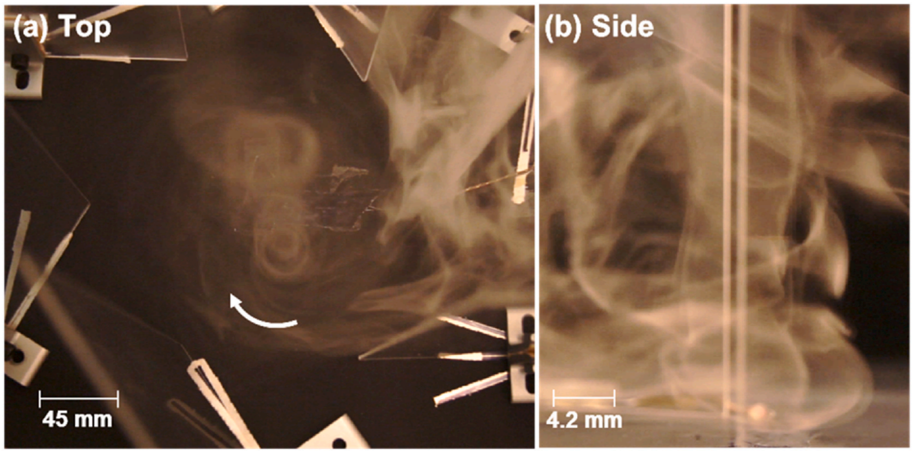

Fig. 13. Fully formed BICV observed from the (a) top and (b) side views. Note that images are not concurrent. Arrow indicates clockwise rotation of the flow.

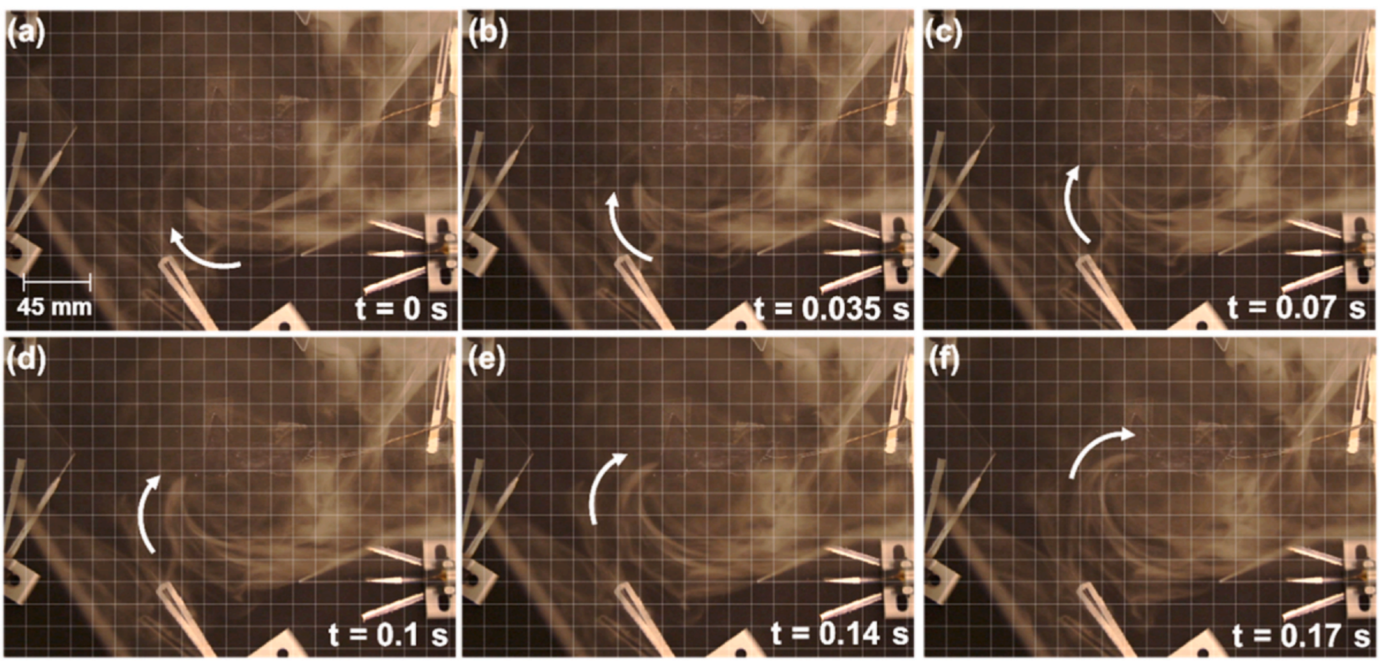

Fig. 14. Flow visualization of BICV highlighting rotation of air. Conditions shown are $L_h = 0.3$ m, $T_p = 100$ °C, and $\theta = 30°$. Arrow indicates clockwise rotation of the flow.

3.5. Preliminary flow visualizations

The FDS results demonstrated that at the small heater size, $L_h = 0.3$ m, similar downward mass fluxes were observed compared to the $L_h = 1$ m case. The small heater and corresponding vane configuration then became the basis for the experimental design (Fig. 5), and an experimental campaign is currently underway to gain further insight on how the flow field of a BICV will impact surrounding smoldering fuel, particularly, how fresh air can be entrained into porous fuel beds such as pine needles and transition to flaming.

Successful and repeatable generation of BICV was achieved at the approximate center of the heated plate and verified using fog visualization. Fig. 13 shows fully developed BICVs with the vortex boundaries and rotational core sharply visualized with the seeded fog. From these images the vortex core diameter can be approximated to be between 1.5 and 2.5 cm, comparable to the 2.4 cm from the FDS results.

The formation of a BICV and consequent vortex rotation is better described by the observations in the top view sequence of images in Fig. 14. Air seeded with fog is entrained from the top right and moves toward the center with a rotational path. The center core region of the rotation becomes increasingly cloudy over time, as fog is entrained and diffused in the center and then transported upwards.

Edge detection was applied (Matlab[1] internal edge detection algorithm with Canny method) to the image sequence to clearly visualize the outlines from the fog. Further processing placed the edge detected binary images in the RGB matrix of an image and color coded the time series such that each color corresponds to a different image frame and time stamp. Fig. 15 shows the color-coded edge detection of a subset of

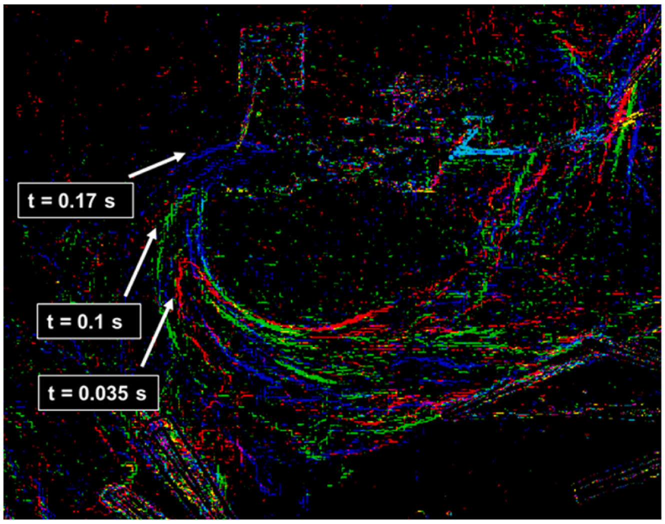

Fig. 15. Composite edge detection image showing the BICV rotation from a top view. The colors correspond to time, progressing from red to green to blue and are taken from Fig. 14b, d, and 14f, respectively. (For interpretation of the references to color in this figure legend, the reader is referred to the Web version of this article.)

the images from Fig. 14 where red corresponds to Fig. 14b, green 14d, and blue 14f. The colorized edge detection facilitates the comparison of image frames and easily shows the rotational motion of the BICV.

Flow visualization was conducted from the side view to document the downward air movement as shown by the image sequence in Fig. 16. The figure shows a sequence of images with a BICV formed approximately at the center of the domain. As the BICV rotates, the bottom right boundary of the air column moves and expands downward. The air continues moving downward until reaching the surface of the heater at which point the air spreads laterally. In order to calculate smoke edge velocity, the camera was calibrated with a millimeter resolution grid target, correlating image pixels to spatial distance. With time between images (framerate) known, a velocity was calculated. By tracking the smoke front, the average downward flow speed is estimated at approximately 1.45 ± 0.22 cm/s. This estimate is comparable to downward vertical velocity in the vicinity of the core region of the FDS simulations. The flow visualization and the FDS contours show that as the air spirals inward, it dives downward and forms the downward entrainment streaks shown in the velocity contours from the simulations (Figs. 6 and 10).

The side view images were similarly analyzed with edge detection to highlight the downward movement of air. Fig. 17 shows the composite edge detection image of Fig. 16a, c, and 16e. Each color channel is separated by approximately 0.07s and clearly shows the progression (red to green to blue) of the air moving downward at the bottom left of the BICV.

4. Conclusions

The use of FDS to model BICV was successfully assessed by conducting simulations utilizing a similar setup to published experimental results. The global behavior agrees with the trends identified in literature. Furthermore, FDS was able to capture both 1-cell and 2-cell vortex regimes. With confidence that FDS could model BICV, simulations were conducted at a smaller benchtop scale. Comparing the flow fields across size scales showed similarities in the air entrainment patterns and downward velocity streaks. However, a 2-cell structure was not achieved at the smaller scale. Crucially, downward mass flux similarity was achieved. It was shown that the formation of a BICV increases the downward mass flux significantly. Ultimately it is the downward mass flux of air that would influence the combustion of smoldering fuel and could lead to a transition to flaming. These results informed the design of an ongoing experimental campaign. Preliminary results show that the design of benchtop experiments was successful as they yielded consistent formation of BICVs. Furthermore, preliminary flow visualization

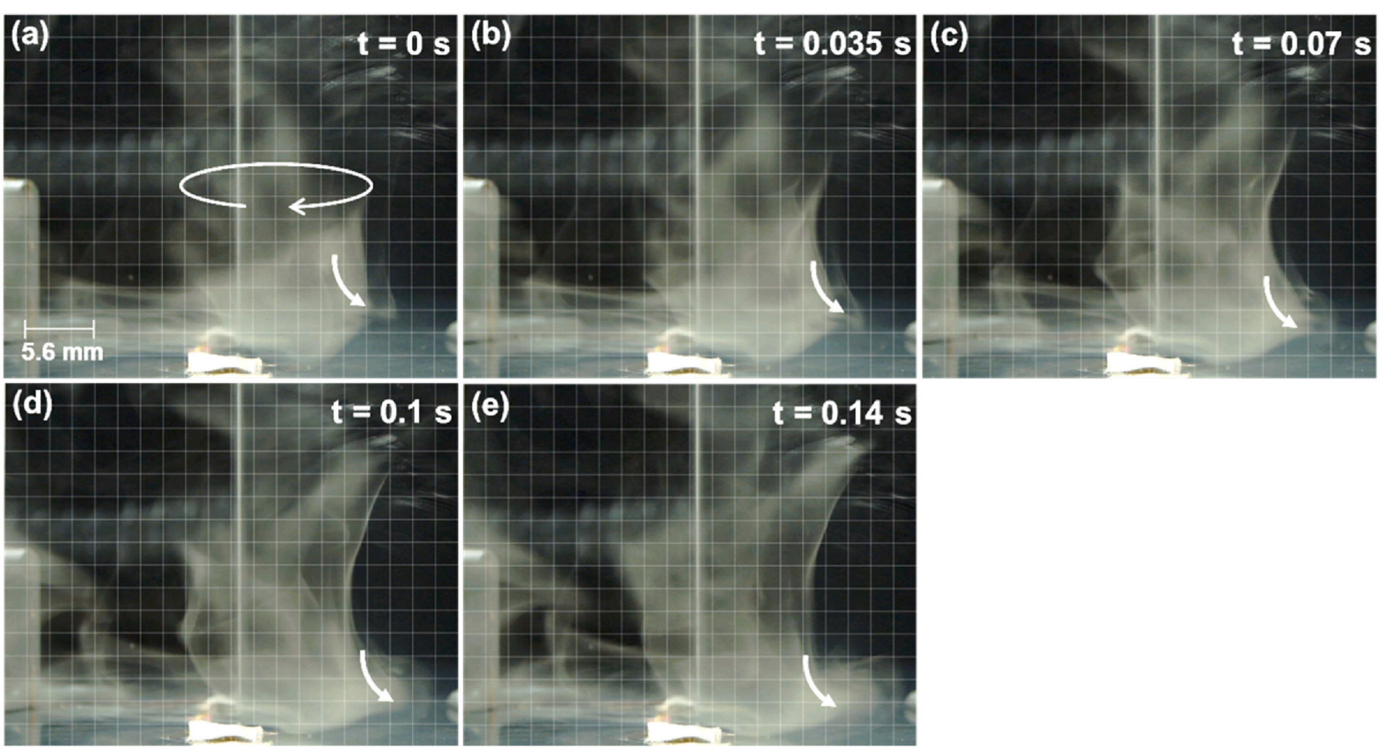

Fig. 16. Flow visualization of BICV highlighting downward movements of air. Conditions shown are $L_h = 0.3$ m, $T_p = 100$ °C, and $\theta = 30°$. Arrow indicates clockwise rotation of the flow.

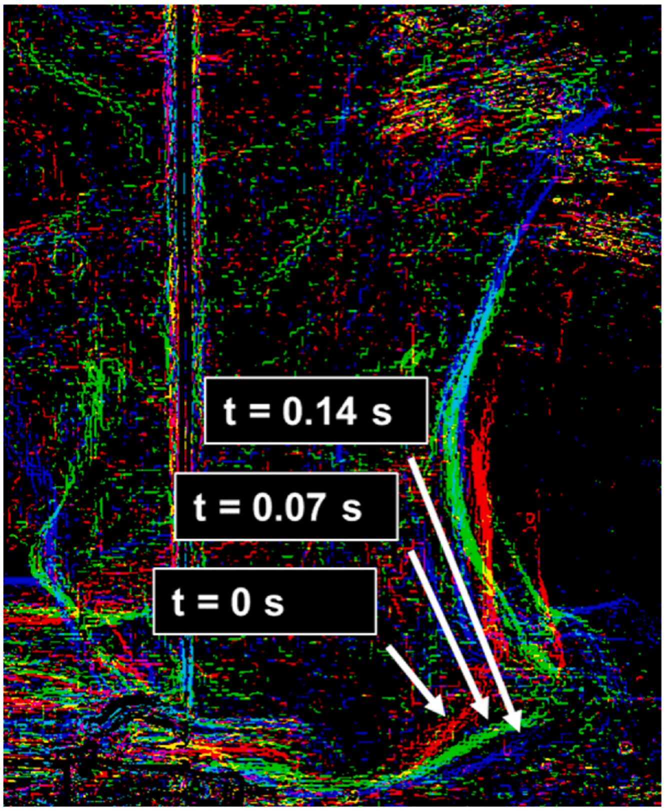

Fig. 17. Composite edge detection image showing the BICV rotation from a side view. The colors correspond to time, progressing from red to green to blue and are taken from Fig. 16a, c, and 16e, respectively. (For interpretation of the references to color in this figure legend, the reader is referred to the Web version of this article.)

highlights some of the key mechanisms by which entrained air may flow downward into a fuel substrate. These flow visualizations show qualitative agreement with the FDS results.

Author statement

Giovanni Di Cristina: Conceptualization, Methodology, Validation, Formal Analysis, Investigation, Writing (Original Draft), Writing (Review & Editing), Visualization. **Rodney A. Bryant**: Methodology, Resources, Writing (Review & Editing), Supervision, Project administration.

Declaration of competing interest

The authors declare that they have no known competing financial interests or personal relationships that could have appeared to influence the work reported in this paper.

Data availability

Data will be made available on request.

References

[1] National Interagency Coordination Center Wildland Fire Summary and Statistics Annual Report, NICC, 2021 n.d. https://www.predictiveservices.nifc.gov/intelligence/2021_statssumm/annual_report_2021.pdf. (Accessed 20 April 2022).

[2] A. Tohidi, M.J. Gollner, H. Xiao, Fire whirls, Annu. Rev. Fluid Mech. 50 (2018) 187–213, https://doi.org/10.1146/annurev-fluid-122316-045209.

[3] D. Rosenfeld, M. Fromm, J. Trentmann, G. Luderer, M.O. Andreae, R. Servranckx, The Chisholm firestorm: observed microstructure, precipitation and lightning activity of a pyro-cumulonimbus, Atmos. Chem. Phys. 7 (2007) 645–659, https://doi.org/10.5194/acp-7-645-2007.

[4] M. Fromm, D.T. Lindsey, R. Servranckx, G. Yue, T. Trickl, R. Sica, P. Doucet, S. Godin-Beekmann, The untold story of pyrocumulonimbus, Bull. Am. Meteorol. Soc. 91 (2010) 1193–1210, https://doi.org/10.1175/2010BAMS3004.1.

[5] S.L. Manzello, S. Suzuki, The importance of combustion science to unravel complex processes for informal settlement fires, urban fires, and wildland-urban interface (WUI) fires, Fuel 314 (2022), 122805, https://doi.org/10.1016/j.fuel.2021.122805.

[6] G. Di Cristina, M.R. Gallagher, N.S. Skowronski, A. Simeoni, A. Rangwala, S. Im, Design and implementation of a portable, large-scale wind tunnel for wildfire research, Fire Saf. J. 131 (2022), 103607, https://doi.org/10.1016/j.firesaf.2022.103607.

[7] H.J. Lugt, Vortex breakdown in atmospheric columnar vortices, Bull. Am. Meteorol. Soc. 70 (1989) 1526–1537, https://doi.org/10.1175/1520-0477(1989)070<1526:VBIACV>2.0.CO;2.

[8] M.W. Simpson, A. Glezer, Buoyancy-induced, columnar vortices, J. Fluid Mech. 804 (2016) 712–748, https://doi.org/10.1017/jfm.2016.541.

[9] J.B. Mullen, T. Maxworthy, A laboratory model of dust devil vortices, Dynam. Atmos. Oceans 1 (1977) 181–214, https://doi.org/10.1016/0377-0265(77)90006-9.

[10] S. Raasch, T. Franke, Structure and formation of dust devil–like vortices in the atmospheric boundary layer: a high-resolution numerical study, J. Geophys. Res. 116 (2011), D16120, https://doi.org/10.1029/2011JD016010.

[11] A.Y. Varaksin, M.E. Romash, V.N. Kopeitsev, M.A. Gorbachev, Experimental study of wall-free non-stationary vortices generation due to air unstable stratification, Int. J. Heat Mass Tran. 55 (2012) 6567–6572, https://doi.org/10.1016/j.ijheatmasstransfer.2012.06.063.

[12] A.Yu Varaksin, M.E. Romash, S.I. Taekin, V.N. Kopeitsev, The generation of free concentrated air vortexes under laboratory conditions, High Temp. 47 (2009) 78–82, https://doi.org/10.1134/S0018151X09010106.

[13] A.Yu Varaksin, M.E. Romash, V.N. Kopeitsev, The possibilities of visualization in the case of simulation of air tornados, High Temp. 48 (2010) 588–592, https://doi.org/10.1134/S0018151X10040176.

[14] M.V. Kurgansky, R.D. Lorenz, N.O. Renno, T. Takemi, Z. Gu, W. Wei, Dust devil steady-state structure from a fluid dynamics perspective, Space Sci. Rev. 203 (2016) 209–244, https://doi.org/10.1007/s11214-016-0281-0.

[15] T. Maxworthy, A vorticity source for large-scale dust devils and other comments on naturally occurring columnar vortices, J. Atmos. Sci. 30 (1973) 1717–1722, https://doi.org/10.1175/1520-0469(1973)030<1717:AVSFLS>2.0.CO;2.

[16] D.E. Fitzjarrald, A field investigation of dust devils, J. Appl. Meteorol. 12 (1973) 808–813, https://doi.org/10.1175/1520-0450(1973)012<0808:AFIODD>2.0.CO;2.

[17] P.C. Sinclair, The lower structure of dust devils, J. Atmos. Sci. 30 (1973) 1599–1619, https://doi.org/10.1175/1520-0469(1973)030<1599:TLSODD>2.0.CO;2.

[18] H.W. Emmons, S.-J. Ying, The fire whirl, Symp. Int. Combust. 11 (1967) 475–488, https://doi.org/10.1016/S0082-0784(67)80172-3.

[19] J. Lei, N. Liu, Reciprocal transitions between buoyant diffusion flame and fire whirl, Combust. Flame 167 (2016) 463–471, https://doi.org/10.1016/j.combustflame.2015.10.009.

[20] S.B. Hariharan, Y. Hu, M.J. Gollner, E.S. Oran, Effects of circulation and buoyancy on the transition from a fire whirl to a blue whirl, Phys. Rev. Fluids. 5 (2020), 103201, https://doi.org/10.1103/PhysRevFluids.5.103201.

[21] M.W. Simpson, SIMPSON-DISSERTATION-2015.pdf, Georgia Institute of Technology, 2015. http://hdl.handle.net/1853/54434.

[22] J.M. Forthofer, S.L. Goodrick, Review of vortices in wildland fire, J. Combust. 2011 (2011) 1–14, https://doi.org/10.1155/2011/984363.

[23] F. Richter, F.X. Jervis, X. Huang, G. Rein, Effect of oxygen on the burning rate of wood, Combust. Flame 234 (2021), 111591, https://doi.org/10.1016/j.combustflame.2021.111591.

[24] W. Coenen, E.J. Kolb, A.L. Sánchez, F.A. Williams, Observed dependence of characteristics of liquid-pool fires on swirl magnitude, Combust. Flame 205 (2019) 1–6, https://doi.org/10.1016/j.combustflame.2019.03.032.

[25] M. Shinohara, Vortex strength and size of fire whirls without flames around a long narrow fire source, Fire Saf. J. 129 (2022), 103561, https://doi.org/10.1016/j.firesaf.2022.103561.

[26] K.B. McGrattan, Fire Dynamics Simulator (Version 4) :: Technical Reference Guide, 0 ed., National Institute of Standards and Technology, Gaithersburg, MD, 2006 https://doi.org/10.6028/NIST.SP.1018.

[27] K.B. McGrattan, G.P. Forney, Fire Dynamics Simulator (Version 4) :: User's Guide, 0 ed., National Institute of Standards and Technology, Gaithersburg, MD, 2004 https://doi.org/10.6028/NIST.SP.1019.